

Templated Solvent-Free Powder Synthesis and MOF-CVD Films of the Ultramicroporous Metal–Organic Framework α -Magnesium Formate

Dmitry E. Kravchenko, Alexander John Cruz, Sabina Rodríguez-Hermida, Nathalie Wauteraerts, Tom Hauffman, and Rob Ameloot*



Cite This: <https://dx.doi.org/10.1021/acs.chemmater.0c03212>



Read Online

ACCESS |



Metrics & More



Article Recommendations



Supporting Information

ABSTRACT: Because of their molecular sieving properties, metal–organic frameworks have a high potential for application in gas storage, separation, and sensing. However, their real-world implementation will require robust and low-cost synthetic approaches. We herein report the solvent-free synthesis of ultramicroporous α -magnesium formate (α -MgFm) based on the solid–vapor reaction of magnesium oxide (MgO) and formic acid and establish the requirement for a structure-directing agent. Translated into a chemical vapor deposition protocol, this method enables the fabrication of high-quality, pinhole-free films of α -MgFm.



Metal–organic frameworks (MOFs) are microporous crystalline coordination polymers built from metal ion nodes connected by organic linkers.¹ Because of their defined pore structure and a functionalizable pore interior, these materials have received much attention in gas storage, separation, and sensing.^{1,2} MOFs with pores of width approximately no more than two or three molecular diameters (i.e., below 5–7 Å) are called ultramicroporous.³ They display remarkable selectivity between small molecules with similar physical and chemical properties.⁴ For instance, the adsorptive separation of C₂H₂ and C₂H₄, with respective kinetic diameters of 3.3 and 4.16 Å, was achieved using an ultramicroporous calcium squarate MOF (pore size: 3.4 Å).⁵ At least as impressive is the selective adsorption of CO₂ over C₂H₂, both with a kinetic diameter of 3.3 Å, on ultramicroporous pillared SIFSIX-3-Ni (3.8 Å).⁶

The application of these MOFs in sensing and membrane-based gas separation requires a convenient way to deposit high-quality thin films. To the best of our knowledge, only two pure ultramicroporous MOF films have been reported so far. Ni₂(L-aspartate)₂pyrazine (JUC-150, pore size: 2.5 × 4.5 Å) was grown on a sacrificial nickel mesh under solvothermal conditions.⁷ Solvothermal growth is neither favorable for manufacturing sensing devices nor does it easily yield high-quality films. Because of the fast diffusion of both metal ions and linkers in solution, there is little control over nucleation and growth rates, which often leads to the formation of scattered crystallites instead of thin, pinhole-free thin films. Another example is the liquid-phase epitaxial growth of a SIFSIX-3-Ni membrane.⁸ The fabrication of a virtually defect-free membrane took 30 growth cycles, leading to a rough and thick (5 μm) MOF film.

Recently, our group demonstrated the chemical vapor deposition of MOFs (MOF-CVD) for the solvent-free growth of high-quality thin films.^{9–11} This all-vapor-phase approach consists of two steps: (1) deposition of a precursor film, typically a metal oxide, and (2) precursor-to-MOF conversion by exposure to linker vapor. Herein, we demonstrate MOF-CVD of high-quality α -magnesium formate [Mg₃(HCOO)₆] (α -MgFm) films by the reaction of sputtered MgO with formic acid vapor.

Anhydrous magnesium formate (MgFm) exists in at least three polymorphs: as α ,¹² β ,¹³ and γ ¹⁴-magnesium formate. While the β -phase is a dense coordination polymer, the α - and γ -phases demonstrate permanent porosity.^{14,15} Both porous polymorphs have similar topologies and accessible surface areas but form in the presence of different structure-directing agents (SDAs): *N,N*-dimethylformamide (DMF) for α -MgFm and 1,3-benzeneditetrazole for γ -MgFm. Interestingly, as DMF decomposes to formic acid when heated in the presence of moisture, it can serve as a linker precursor in α -MgFm synthesis.¹⁶ The much higher volatility of DMF compared to that of 1,3-benzeneditetrazole makes α -MgFm a promising candidate for MOF-CVD.

Magnesium oxide (MgO) was selected as a precursor because of its reactive nature and ease of sputter deposition.

Received: August 5, 2020

Revised: November 6, 2020

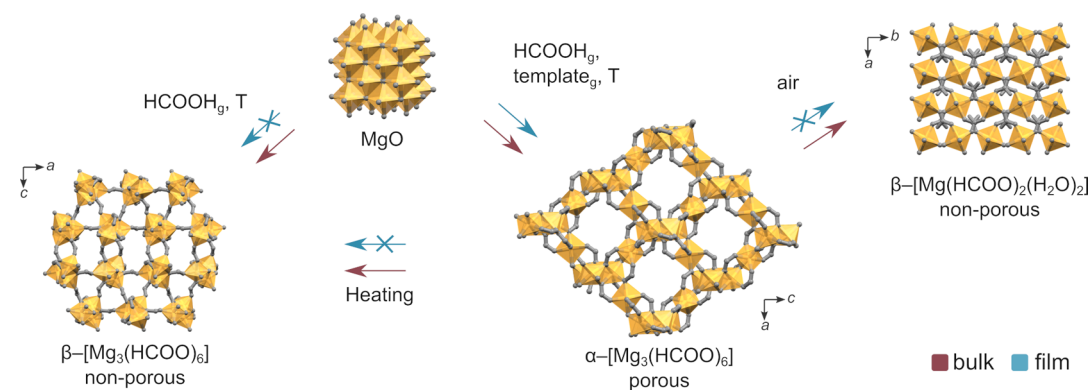


Figure 1. Products resulting from the reaction of formic acid vapor with MgO, in both bulk powder and thin-film forms.

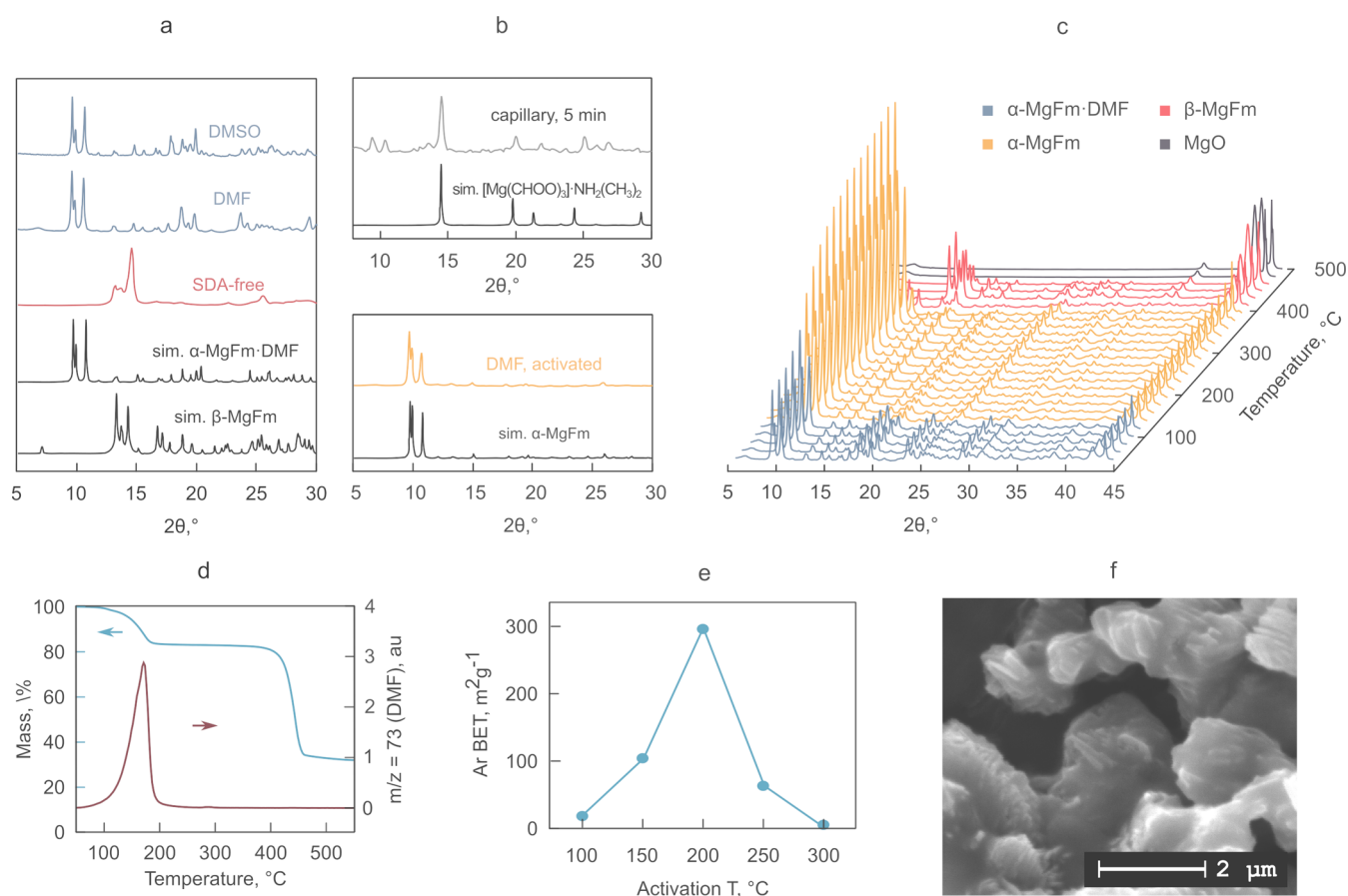


Figure 2. Synthesis and characterization of magnesium formate (MgFm) powder. (a) PXRD patterns of products obtained by the reaction of MgO with formic acid vapor, with and without DMF or DMSO added as an SDA. (b, top) PXRD data illustrating the formation of perovskite-like $[\text{Mg}(\text{CHOO})_3]\cdot\text{NH}_2(\text{CH}_3)_2$ in the early stages of reaction in the presence of DMF. (b, bottom) PXRD data of $\alpha\text{-MgFm}$ after activation. (c) Activation study of the as-synthesized $\alpha\text{-MgFm}\cdot\text{DMF}$ via VT-PXRD. (d) TG–MS analysis of $\alpha\text{-MgFm}\cdot\text{DMF}$. (e) Ar BET surface area measured at 77 K for $\alpha\text{-MgFm}$ activated at different temperatures. (f) SEM image of as-synthesized $\alpha\text{-MgFm}\cdot\text{DMF}$.

Before proceeding to thin films, the bulk reaction between MgO powder and formic acid vapor was studied. Bulk samples allow the straightforward use of characterization techniques such as thermogravimetry (TG), mass spectrometry (MS), and gas physisorption. In addition, the solvent-free conversion of MgO is valuable on its own as a low-cost, environmentally friendly method for bulk $\alpha\text{-MgFm}$ production. The reaction of MgO with formic acid vapor leads to different products, depending on the presence or absence of a template (Figure 1). In the absence of an SDA, the nonporous $\beta\text{-MgFm}$ is formed at 150 °C (Figure 2a, red). To facilitate the formation

of the porous $\alpha\text{-MgFm}$ phase, several organic solvent vapors were tested as potential SDAs: DMF, dimethyl sulfoxide (DMSO), tetrahydrofuran, 1,4-dioxane, 2-methylfuran, and cyclohexane (Figure S1). Special care was taken to ensure full vaporization during synthesis to avoid solid–liquid reactions. Formic acid and the SDA were added to the reaction chamber in such amounts that their partial pressures after full evaporation were equal to approximately 0.3 bar, which are lower than their saturation pressure at the reaction temperature. While most tested SDAs led to amorphous products, DMSO and DMF directed the reaction toward the desired $\alpha\text{-}$

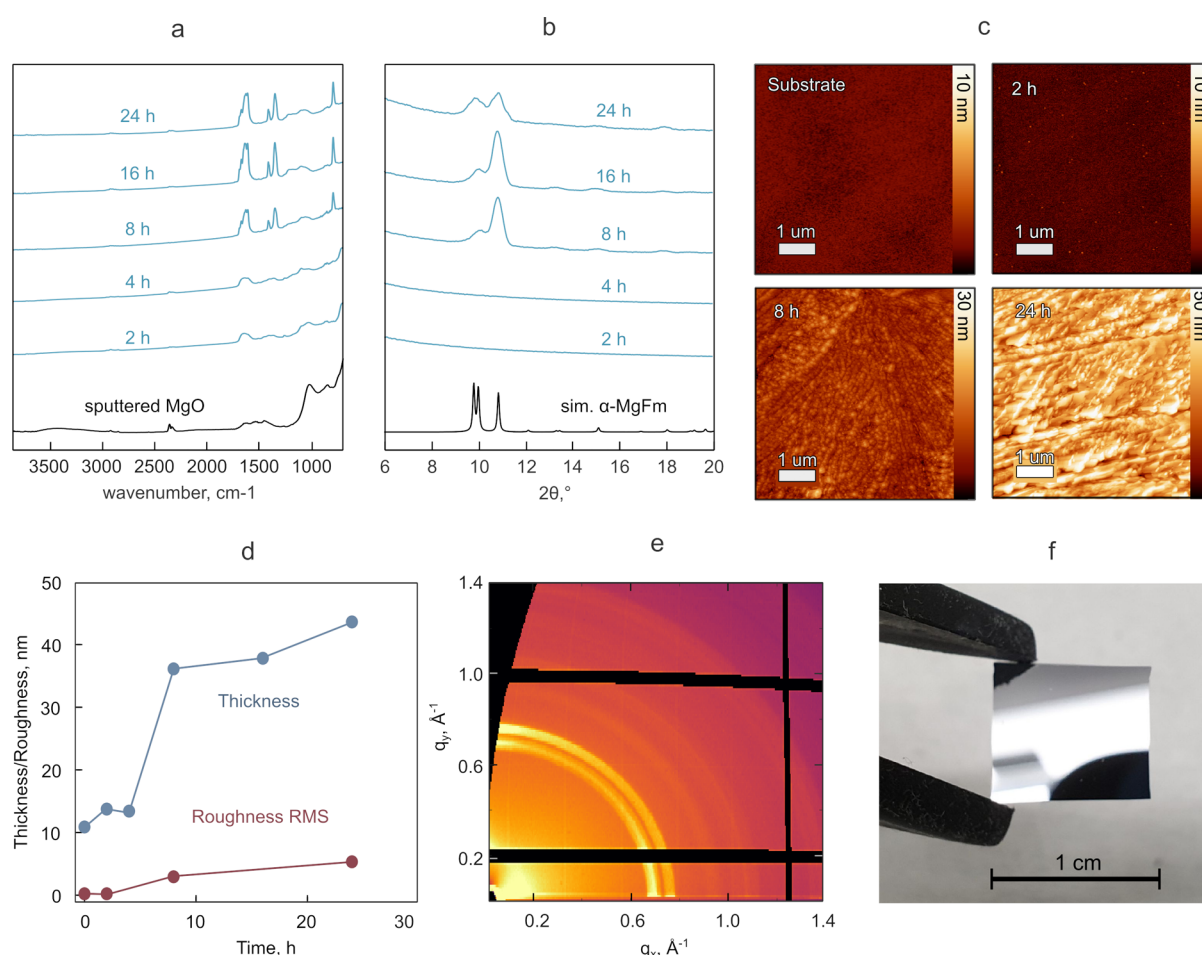


Figure 3. Synthesis and characterization of α -MgFm films. FTIR spectra (a) and GIXRD patterns (b) of sputtered MgO exposed to formic acid and DMF vapors for different times. (c) AFM snapshots at different reaction times. (d) Layer thickness and roughness as a function of reaction time. The thickness was derived from ellipsometry using appropriate models.¹⁸ The rms roughness from a $6 \times 6 \mu\text{m}^2$ area was probed by AFM. (e) Synchrotron GIXRD pattern after 8 h of reaction. (f) Photograph of the film after 8 h of conversion.

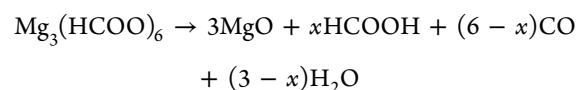
MgFm-DMF and α -MgFm-DMSO phases (Figure 2a, blue). The obtained α -MgFm-DMF is composed of coalesced submicrometer crystallites (Figure 2f).

The time-resolved formation of α -MgFm-DMF in a sealed capillary was studied by XRD with synchrotron radiation (Figure S2). At first, traces of dense perovskite-like phase $[\text{Mg}(\text{CHOO})_3] \cdot \text{NH}_2(\text{CH}_3)_2$ were observed (Figure 2b, top). This material is isostructural to the previously reported Mn, Co, and Ni compounds¹⁷ and forms, thanks to the partial decomposition of DMF to dimethylamine. After a few minutes, α -MgFm-DMF starts crystallizing and quickly becomes the predominant phase. Attempts to isolate the perovskite-like compound were not successful.

The reported specific surface area values of α -MgFm vary from 150¹⁵ and 284¹⁸ to 496^{16,19} $\text{m}^2 \text{g}^{-1}$. This striking discrepancy is seemingly due to slightly different unit cell parameters of the samples prepared via different synthesis routes¹⁶ and, more importantly, via different activation procedures. To find the optimal activation temperature for α -MgFm-DMF, variable temperature powder X-ray diffraction (VT-PXRD) measurements were performed (Figure 2c). A clear change in the relative peak intensities caused by the changes in the in-pore electron density is observed at 150 °C. The room-temperature and 150 °C powder patterns match with the simulated PXRD patterns for the DMF-loaded

(Cambridge Structural Database (CSD) reference code: NAXVOY01) and evacuated structures (CSD: XEHSUZ), respectively. This finding confirms the successful evacuation of the DMF guest molecules from the pores. The activated framework is stable up to 350–400 °C in air. At higher temperatures, it undergoes a phase transition to the nonporous β -MgFm. Between 400 and 450 °C, the β -phase gradually decomposes, as can be seen from the increasing MgO diffraction peaks at 43 and 44° 2θ .

The activation and thermal stability of α -MgFm-DMF were studied further by simultaneous TG in air and MS (Figure 2d). As expected, the TG profile consists of two mass loss steps: desorption of DMF at 120–190 °C and thermal decomposition at 420–460 °C. The activation step is accompanied by the release of DMF ($m/z = 73$), with a peak at 170 °C. This result confirms the presence of DMF in the pores and supports its role as an SDA. Thermal decomposition is nonoxidative as the TG profiles measured in air and nitrogen overlap (Figure S3). The release of both water and formic acid (Figure S4) suggests the following mechanism



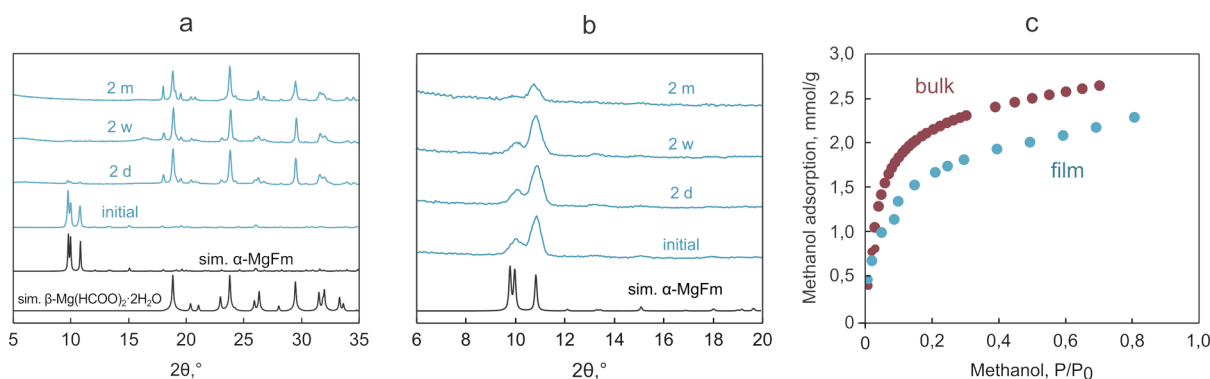


Figure 4. Stability in a humid atmosphere (RH = 33%) and the porosity of α -MgFm powder and films. (a) PXRD patterns of the bulk powder and (b) GIXRD patterns of the thin film immediately after activation and after storage for 2 days, 2 weeks, and 2 months. (c) Methanol adsorption isotherms of the α -MgFm powder and film at 25 °C. The powder and film samples were activated at 200 and 120 °C, respectively.

The porosity of α -MgFm was studied by argon physisorption. The choice of argon over nitrogen as a probe molecule is due to the smaller probe size, higher symmetry, and absence of quadrupole moment, which is advantageous to polar microporous solids.²⁰ α -MgFm was activated at different temperatures for 8 h under dynamic vacuum (Figure 2e). The highest BET surface area was found for activation at 200 °C. While milder activation is not sufficient to remove all DMF from the pores, heating α -MgFm to higher temperatures for a prolonged time causes partial pore collapse. The BET area of 297 m² g⁻¹ is in good agreement with the previously reported value of 284 m² g⁻¹ for solvothermal synthesis.¹⁴ However, it falls short of 496 m² g⁻¹ reported for α -MgFm with an expanded unit cell using supercritical CO₂ for activation.¹⁶

The optimized conversion conditions to obtain the α -MgFm powder were tested on a 10 nm MgO film sputtered on a wafer substrate. The samples were placed in a reaction chamber, together with formic acid and DMF, and heated to 150 °C for 3 days. Unexpectedly, the conditions for bulk powder conversion were not directly applicable to thin films, as no crystalline product was formed. Two possible reasons can account for these observations. First, there is considerable depletion of formic acid and DMF vapor, as well as the release of water, during the bulk synthesis, which might shift the thermodynamic equilibrium in favor of α -MgFm. In contrast, these changes are negligible in the case of thin films because of the much lower quantity of MgO present in the chamber. Second, sputtered MgO converts to Mg(OH)₂ and MgCO₃ when exposed to ambient air before the experiment, as indicated by Fourier-transform infrared (FTIR) spectroscopy and XPS data (Figures S5 and S6), and this conversion affects its reactivity.

Different conditions were tested for α -MgFm film formation, by varying the time, temperature, and amounts of formic acid and DMF. Highly crystalline and smooth films of α -MgFm were obtained under milder conditions compared to bulk powder conversion: 100 °C, 0.02 bar formic acid, 0.1 bar DMF, and 8 h reaction time. Figure 3 summarizes a detailed study on the kinetics of conversion. As indicated by the appearance of symmetric and asymmetric carboxylate stretching bands at 1640 and 1350–1450 cm⁻¹, the reaction between the metal source and formic acid starts already after 2 h. However, at this stage, the film is amorphous and its thickness remains virtually unchanged. The film thickness is an indicator of the degree of MgO conversion and is expected to increase drastically when the dense metal precursor converts to a

porous MOF.²¹ In the case of α -MgFm, the theoretical film expansion factor, as calculated from the corresponding molar volumes, equals 7.3 \times , 3.3 \times , and 3.0 \times when using MgO, Mg(OH)₂, and MgCO₃ as precursors, respectively (see Table S1 for details). Between 4 and 8 h, α -MgFm crystallizes, as evidenced by the corresponding XRD reflections, changes in the FTIR spectrum, and considerable film expansion. At 8 h, the film expands 3.2 times, which is in good agreement with the theoretical values of both Mg(OH)₂ and MgCO₃. Also, a thicker 20 nm MgO film was successfully converted to α -MgFm under the same conditions. The identical expansion factor of 3.2 indicates that also in this case full conversion was reached (Figures S7 and S8). Both films were found to be pinhole-free, as evidenced by conductive atomic force microscopy (AFM) and even for a bias voltage of 10 V (Figure S9). Prolonged reaction time leads to an increase in particle size and roughness, likely due to ripening. As evidenced by AFM (Figure 3c), the root-mean-square (rms) roughness increases from 2.9 nm at 8 h to 7.4 nm at 24 h. Moreover, the film gradually loses its crystallinity as the XRD reflections broaden with reaction time, indicating the metastability of the α -MgFm phase. Overall, the observed behavior bears a strong resemblance to the MOF-CVD of ZIF-8: a metal oxide reacts with the linker forming an amorphous product, which crystallizes into a MOF after an induction period.²¹ However, compared to ZIF-8, the formation of α -MgFm films is considerably slower.

In contrast to the bulk powder, the film does not undergo phase transition from α - to β -MgFm upon heating (Figure S10). Moreover, the thin film demonstrates superior thermal stability, up to 400 °C and even for a prolonged time. The same holds for its stability in the presence of humidity: while bulk α -MgFm converts into nonporous β -[Mg₃(HCOO)₆·2H₂O] (CSD: BEWFOY) after only a few hours of exposure to ambient air, the thin film is stable for at least several weeks (Figure 4a,b). A possible explanation for this phenomenon is a strain-induced stabilization that occurs only in thin films. A similar effect was recently demonstrated to stabilize thin films of metastable CsPbI₃ perovskites.²²

Adsorption of methanol at 25 °C was measured to compare the porosity of α -MgFm powder and films. For the powder, the uptake was measured volumetrically, by an automated gas physisorption instrument. For thin-film measurements, MgO (10 nm) was sputtered on a quartz crystal microbalance (QCM) sensor, followed by the established MOF-CVD protocol. The difference between the resonance frequency of

the sensor before and after MOF deposition was used to calculate the mass of the α -MgFm film. The sensor was placed in a miniature flow chamber and its resonance frequency was measured at different concentrations of methanol vapor. By exploiting the direct proportionality between the adsorbed mass and the frequency shift, methanol uptake ($\text{mmol}\cdot\text{g}^{-1}$) was calculated. Both isotherms exhibit a type I behavior, with the adsorption capacity of the film being only slightly lower (Figure 4). The pore volume was determined from the uptake at $P/P_0 = 0.7$ and assuming the density of liquid methanol for the adsorbed phase. The resulting values of 0.11 and 0.09 cm^3 g^{-1} for the bulk powder and the thin film, respectively, are in good agreement with 0.10 cm^3 g^{-1} measured for α -MgFm powder by Ar physisorption.

In conclusion, this work has expanded the MOF-CVD method to the ultramicroporous MOF α -MgFm. The crucial role of the SDA for solvent-free synthesis of this MOF was demonstrated for both powder formation and thin-film deposition. Grazing incidence X-ray diffraction (GIXRD), together with ellipsometry, AFM topography scans, and conductive AFM show that the resulting films are smooth, of high quality, and pinhole-free. Contrary to expectations, thin films of α -MgFm fabricated via MOF-CVD were shown to be both more thermally and moisture stable in comparison with bulk powders.

MATERIALS AND METHODS

Chemicals. MgO (extra pure, Acros Organics); formic acid (99–100%, Chem-Lab Analytical bvba); DMF (99+%, extra pure, Acros Organics); DMSO (99.7+%, Actos Organics); tetrahydrofuran (99+%, extra pure, stabilized, Acros Organics); 1,4-dioxane (99.5%, for analysis, stabilized, Acros Organics); 2-methylfuran (99%, Actos Organics); and cyclohexane (99+%, pure, Acros Organics).

Substrates. Single-side polished back-etched p-type Si wafers oriented along the $\langle 100 \rangle$ axis (Si-Mat Silicon Materials, Germany) were used as a substrate. Their diameter was 76.2 mm, thickness was 381 ± 25 μm , and resistivity was 1 – 30 $\Omega\cdot\text{cm}$. To measure methanol adsorption on a thin film, a gold-coated 6 MHz quartz crystal (Inficon, 008-010-G10) was used as a substrate.

MgO Deposition. MgO thin films were deposited through physical vapor deposition with a BAE370 magnetron RF sputter coater, using a MgO target (99.999% purity, Demaco). The depositions were done at a pressure of $\sim 2 \times 10^{-3}$ mbar, under an Ar plasma, at power set to 150 W for 3 min. The target thickness of 10 nm was confirmed by ellipsometry.

Bulk Powder Synthesis. For the typical solvent-free synthesis of bulk powder of α -MgFm, 40.3 mg (1.0 mmol) of magnesium oxide, 94.3 μL (2.5 mmol) of formic acid, and 2.5 mmol of an SDA, if present, were placed separately in a 300 mL glass reactor and sealed. The reactor was placed in a forced convection oven preheated at 150 $^\circ\text{C}$ and kept for 3 days.

Thin-Film Deposition. For the optimized procedure, a substrate with a layer of sputtered MgO was placed in a 300 mL glass reactor together with 7.76 μL of formic acid and 79.6 μL of DMF or 73.2 μL of DMSO. The partial pressures of formic acid and DMF after full evaporation were equal to approximately 0.3 bar, which are lower than their saturation pressure at the reaction temperature. The reactor was placed in a forced convection oven preheated at 100 $^\circ\text{C}$ at a specific duration. At the end of the reaction time, the sample was removed from the reactor and allowed to cool down in air.

It should be noted that both DMF and DMSO can decompose upon heating, and this process can be accelerated by other compounds present (e.g., formic acid).^{23,24} However, as both DMF and DMSO act as SDAs in our case, only very small amounts are used, and this decomposition does not present a safety issue. For instance, even if all added DMSO would decompose, thereby yielding two volatile molecules per molecule of DMSO (i.e., formaldehyde and

methyl sulfide), the pressure in the reactor would increase only by 0.6 bar and would remain in a safe regime.

Powder X-ray Diffraction. PXRD patterns were recorded with a Malvern PANalytical Empyrean diffractometer in transmission mode over the 3 – 40 2θ range, using a PIXcel3D solid-state detector and a Cu anode (Cu $K\alpha_1$: 1.5406 \AA ; Cu $K\alpha_2$: 1.5444 \AA). Temperature-dependent PXRD patterns were recorded on the same diffractometer in an Anton Paar TTK 600 chamber in reflection mode on a powder bed in air. The temperature was increased by 5 $^\circ\text{C}$ increments and kept constant for 30 min during each measurement.

The capillary experiment was performed on the P02.1 beamline at the Synchrotron DESY (Hamburg, Germany) using a PerkinElmer XRD1621 detector with a photon energy of 60 keV at a wavelength of 0.207 \AA . One-third of the 1.0 mm capillary was first filled with MgO powder, then a thinner 0.8 mm capillary was filled with about 10 μL of $1:1$ M mixture of formic acid and DMF and placed in the thicker capillary, which was sealed with a torch.

Grazing-Incidence X-ray Diffraction. GIXRD measurements were performed on the XRD1 beamline at the Synchrotron Elettra, Trieste, Italy, using a stationary Pilatus 2M detector placed at approximately 400 mm distance from the sample. Data were collected at a wavelength of 1.4 \AA and an incident angle of approximately 0.2 $^\circ$. For the VT-GIXRD measurements, the sample was heated by a nitrogen heating gun at a rate of 5 $^\circ\text{C}\cdot\text{min}^{-1}$. To prevent radiation damage, the sample holder was moved 0.1 mm in the y -axis direction after every scan. To make the measured data comparable, they were transformed into reciprocal space. All data conversion, treatment, and analysis steps were performed with GIDVis.²⁵

Scanning Electron Microscopy. Top-view scanning electron microscopy (SEM) images were recorded using a Philips XL30 FEG microscope (SE detector) operating at an accelerating voltage of 10.0 kV. The samples were cleaved and then sputter-coated with 5 nm of Pt prior to inspection.

Atomic Force Microscopy. Samples were scanned using a PicoSPM (5500, Agilent Technologies) under ambient conditions, in tapping mode using Si cantilevers (AC160TS-R3). Data processing and analysis were carried out with WSXM 5.0.²⁶

Attenuated Total Reflectance-FTIR Spectroscopy. Infrared spectra were recorded (128 scans, 4 cm^{-1} resolution) over the spectral range 750 – 4000 cm^{-1} on a Varian 670 FTIR spectrometer attached to a Varian 620 FTIR microscope equipped with a slide-on Ge ATR tip.

Ellipsometry. The optical properties of the deposited layers were measured using an M-2000x spectroscopic ellipsometer (J. A. Woollam Co., Inc., $\lambda = 246$ – 1000 nm) and using appropriate models.²¹

Profilometry. Contact profilometry was performed on a Bruker's DektakXT Stylus Profiler with a 2 μm stylus, in 6.5 μm stylus scan range and under 5 mg stylus force.

Conductive AFM. To check for pinholes in the MgFm films, conductive AFM was performed using a Dimension Icon system (Bruker) on the MOF layers deposited on p-doped Si substrates. Using a custom holder, the samples were electrically contacted with Ag paint. With a heavily doped full diamond tip, current scans were performed at an applied DC bias voltage of 10.0 V. In our previous work, the threshold bias voltage for the MOF coatings was typically ~ 5.0 V.²¹ Conductive AFM measurements were carried out in a glovebox under an inert (Ar) atmosphere.

Thermogravimetry–Mass Spectrometry. TG analysis was carried out in air using a Netzsch STA 449 F3 Jupiter thermogravimetric analyzer at a heating rate of 5 $^\circ\text{C}\cdot\text{min}^{-1}$. A mass spectrometer (Hiden, HPR-20 QIC–EGA) was coupled to the exhaust line of the TG analyzer. The channels corresponding to $m/z = 18$, 46 , and 73 were monitored.

Volumetric Porosimetry. Ar and methanol physisorption on bulk powder was performed using a Micromeritics 3Flex 3500 instrument at -196 and 25 $^\circ\text{C}$, respectively. Prior to the measurement, the samples were activated at the temperature mentioned in the article for 8 h.

QCM Porosimetry. Adsorption measurements were performed in a custom-made QCM environmental cell at 25 °C. Controlled amounts of methanol were evaporated using a Controlled Evaporator Mixer (Bronkhorst) in a set nitrogen carrier gas flow to obtain methanol vapor of desired concentration. The methanol vapor concentration was varied stepwise in the range 0–0.8 P/P_0 . At the end of each 120 s step, the average frequency change measured during the last 30 s was calculated and plotted against the corresponding partial pressure value.

■ ASSOCIATED CONTENT

Supporting Information

The Supporting Information is available free of charge at <https://pubs.acs.org/doi/10.1021/acs.chemmater.0c03212>.

Theoretical film expansion calculation, PXRD and time-resolved PXRD patterns, GIXRD patterns, TGA–MS curves, FTIR spectra, XPS spectra, ellipsometry data, conductive AFM measurements, and profilometry data (PDF)

■ AUTHOR INFORMATION

Corresponding Author

Rob Ameloot – Department of Microbial and Molecular Systems, Centre for Membrane Separation, Adsorption, Catalysis and Spectroscopy, KU Leuven, 3001 Leuven, Belgium; orcid.org/0000-0003-3178-5480;
Email: rob.ameloot@kuleuven.be

Authors

Dmitry E. Kravchenko – Department of Microbial and Molecular Systems, Centre for Membrane Separation, Adsorption, Catalysis and Spectroscopy, KU Leuven, 3001 Leuven, Belgium; orcid.org/0000-0001-6404-2486

Alexander John Cruz – Department of Microbial and Molecular Systems, Centre for Membrane Separation, Adsorption, Catalysis and Spectroscopy, KU Leuven, 3001 Leuven, Belgium; Research Group of Electrochemical and Surface Engineering, Department of Materials and Chemistry, Vrije Universiteit Brussel, Brussels 1050, Belgium;
orcid.org/0000-0002-5123-1162

Sabina Rodríguez-Hermida – Department of Microbial and Molecular Systems, Centre for Membrane Separation, Adsorption, Catalysis and Spectroscopy, KU Leuven, 3001 Leuven, Belgium; orcid.org/0000-0001-7671-9925

Nathalie Wauteraerts – Department of Microbial and Molecular Systems, Centre for Membrane Separation, Adsorption, Catalysis and Spectroscopy, KU Leuven, 3001 Leuven, Belgium

Tom Hauffman – Research Group of Electrochemical and Surface Engineering, Department of Materials and Chemistry, Vrije Universiteit Brussel, Brussels 1050, Belgium;
orcid.org/0000-0002-3456-0271

Complete contact information is available at:
<https://pubs.acs.org/10.1021/acs.chemmater.0c03212>

Notes

The authors declare no competing financial interest.

■ ACKNOWLEDGMENTS

This project received funding from European Union's Horizon 2020 Research and Innovation Program under the FETOPEN-1-2016-2017 grant agreement no. 801464 (project acronym: SPRINT) and from the European Research Council (ERC)

under grant agreement no. 716472 (acronym: VAPORE). We acknowledge the Marie Skłodowska Curie Training Network HYCOAT, grant agreement 765378, for financial support. We thank the Research Foundation Flanders (FWO Vlaanderen) for research projects G083016N, G0E6319N, and 501618N, and for a SB-PhD fellowship 1SB7919N, as well as KU Leuven for the research project C32/18/056. We acknowledge the Elettra Synchrotron Trieste for allocation of beamtime and thank Luisa Barba and Nicola Demitri for assistance in using beamline XRD1 (20190028). We acknowledge DESY (Hamburg, Germany), a member of the Helmholtz Association HGF, for the provision of experimental facilities and thank Michael Wharmby for assistance in using the P02.1 beamline (I-20180033 EC). We would like to thank IMEC for scientific support, especially Jill Serron and Lennaert Wouters for conductive AFM measurements.

■ REFERENCES

- (1) Furukawa, H.; Cordova, K. E.; O'Keeffe, M.; Yaghi, O. M. The Chemistry and Applications of Metal–Organic Frameworks. *Science* **2013**, *341*, 1230444.
- (2) Stassen, I.; Burtch, N.; Talin, A.; Falcaro, P.; Allendorf, M.; Ameloot, R. An Updated Roadmap for the Integration of Metal–Organic Frameworks with Electronic Devices and Chemical Sensors. *Chem. Soc. Rev.* **2017**, *46*, 3185–3241.
- (3) Thommes, M.; Kaneko, K.; Neimark, A. V.; Olivier, J. P.; Rodriguez-Reinoso, F.; Rouquerol, J.; Sing, K. S. W. Physisorption of Gases, with Special Reference to the Evaluation of Surface Area and Pore Size Distribution (IUPAC Technical Report). *Pure Appl. Chem.* **2015**, *87*, 1051–1069.
- (4) Adil, K.; Belmabkhout, Y.; Pillai, R. S.; Cadiau, A.; Bhatt, P. M.; Assen, A. H.; Maurin, G.; Eddaoudi, M. Gas/Vapour Separation Using Ultra-Microporous Metal–Organic Frameworks: Insights into the Structure/Separation Relationship. *Chem. Soc. Rev.* **2017**, *46*, 3402–3430.
- (5) Li, L.; Guo, L.; Pu, S.; Wang, J.; Yang, Q.; Zhang, Z.; Yang, Y.; Ren, Q.; Alnemrat, S.; Bao, Z. A Calcium-Based Microporous Metal–Organic Framework for Efficient Adsorption Separation of Light Hydrocarbons. *Chem. Eng. J.* **2019**, *358*, 446–455.
- (6) Chen, K.-J.; Scott, H. S.; Madden, D. G.; Pham, T.; Kumar, A.; Bajpai, A.; Lusi, M.; Forrest, K. A.; Space, B.; Perry, J. J.; Zaworotko, M. J. Benchmark C_2H_2/CO_2 and CO_2/C_2H_2 Separation by Two Closely Related Hybrid Ultramicroporous Materials. *Chem* **2016**, *1*, 753–765.
- (7) Kang, Z.; Xue, M.; Fan, L.; Huang, L.; Guo, L.; Wei, G.; Chen, B.; Qiu, S. Highly Selective Sieving of Small Gas Molecules by Using an Ultra-Microporous Metal–Organic Framework Membrane. *Energy Environ. Sci.* **2014**, *7*, 4053–4060.
- (8) Chernikova, V.; Shekha, O.; Belmabkhout, Y.; Eddaoudi, M. Nanoporous Fluorinated Metal–Organic Framework-Based Membranes for CO_2 Capture. *ACS Appl. Nano Mater.* **2020**, *3*, 6432.
- (9) Stassen, I.; Styles, M.; Greci, G.; Gorp, H. V.; Vanderlinden, W.; Feyter, S. D.; Falcaro, P.; Vos, D. D.; Vereecken, P.; Ameloot, R. Chemical Vapour Deposition of Zeolitic Imidazolate Framework Thin Films. *Nat. Mater.* **2016**, *15*, 304–310.
- (10) Stassin, T.; Rodríguez-Hermida, S.; Schrode, B.; Cruz, A. J.; Carraro, F.; Kravchenko, D.; Creemers, V.; Stassen, I.; Hauffman, T.; De Vos, D.; Falcaro, P.; Resel, R.; Ameloot, R. Vapour-Phase Deposition of Oriented Copper Dicarboxylate Metal–Organic Framework Thin Films. *Chem. Commun.* **2019**, *55*, 10056–10059.
- (11) Stassin, T.; Stassen, I.; Marreiros, J.; Cruz, A. J.; Verbeke, R.; Tu, M.; Reinsch, H.; Dickmann, M.; Egger, W.; Vankelecom, I. F. J.; De Vos, D. E.; Ameloot, R. Solvent-Free Powder Synthesis and MOF-CVD Thin Films of the Large-Pore Metal–Organic Framework MAF-6. *Chem. Mater.* **2020**, *32*, 1784–1793.
- (12) Viertelhaus, M.; Adler, P.; Clérac, R.; Anson, C. E.; Powell, A. K. Iron(II) Formate $[Fe(O_2CH)_2] \cdot 1/3HCO_2H$: A Mesoporous

Magnet – Solvothermal Syntheses and Crystal Structures of the Isomorphous Framework Metal(II) Formates $[M(O_2CH)_2]_n$ (Solvent) (M = Fe, Co, Ni, Zn, Mg): Iron(II) Formate $[Fe(O_2CH)_2] \cdot 1/3HCO_2H$: A Mesoporous Magnet. *Eur. J. Inorg. Chem.* **2005**, *2005*, 692–703.

(13) Viertelhaus, M.; Anson, C. E.; Powell, A. K. Solvothermal Synthesis and Crystal Structure of One-Dimensional Chains of Anhydrous Zinc and Magnesium Formate. *Z. Anorg. Allg. Chem.* **2005**, *631*, 2365–2370.

(14) Mallick, A.; Saha, S.; Pachfule, P.; Roy, S.; Banerjee, R. Structure and Gas Sorption Behavior of a New Three Dimensional Porous Magnesium Formate. *Inorg. Chem.* **2011**, *50*, 1392–1401.

(15) Rood, J. A.; Noll, B. C.; Henderson, K. W. Synthesis, Structural Characterization, Gas Sorption and Guest-Exchange Studies of the Lightweight, Porous Metal–Organic Framework α - $[Mg_3(O_2CH)_6]$. *Inorg. Chem.* **2006**, *45*, 5521–5528.

(16) Spanopoulos, I.; Bratsos, I.; Tampaxis, C.; Kourtellaris, A.; Tasiopoulos, A.; Charalambopoulou, G.; Steriotis, T. A.; Trikalitis, P. N. Enhanced Gas-Sorption Properties of a High Surface Area, Ultramicroporous Magnesium Formate. *CrystEngComm* **2015**, *17*, 532–539.

(17) Wang, X.-Y.; Gan, L.; Zhang, S.-W.; Gao, S. Perovskite-like Metal Formates with Weak Ferromagnetism and as Precursors to Amorphous Materials. *Inorg. Chem.* **2004**, *43*, 4615–4625.

(18) Samsonenko, D. G.; Kim, H.; Sun, Y.; Kim, G.-H.; Lee, H.-S.; Kim, K. Microporous Magnesium and Manganese Formates for Acetylene Storage and Separation. *Chem.-Asian J.* **2007**, *2*, 484–488.

(19) Schmitz, B.; Krkljus, I.; Leung, E.; Höffken, H. W.; Müller, U.; Hirscher, M. A High Heat of Adsorption for Hydrogen in Magnesium Formate. *ChemSusChem* **2010**, *3*, 758–761.

(20) Rouquerol, F.; Rouquerol, J.; Sing, K. S. W.; Maurin, G.; Llewellyn, P. Introduction. *Adsorption by Powders and Porous Solids*; Elsevier, 2014; pp 1–24.

(21) Cruz, A. J.; Stassen, I.; Krishtab, M.; Marcoen, K.; Stassin, T.; Rodríguez-Hermida, S.; Teyssandier, J.; Pletincx, S.; Verbeke, R.; Rubio-Giménez, V.; Tatay, S.; Martí-Gastaldo, C.; Meersschant, J.; Vereecken, P. M.; De Feyter, S.; Hauffman, T.; Ameloot, R. Integrated Cleanroom Process for the Vapor-Phase Deposition of Large-Area Zeolitic Imidazolate Framework Thin Films. *Chem. Mater.* **2019**, *31*, 9462–9471.

(22) Steele, J. A.; Jin, H.; Dovgaliuk, I.; Berger, R. F.; Braeckvelt, T.; Yuan, H.; Martin, C.; Solano, E.; Lejaeghere, K.; Rogge, S. M. J.; Notebaert, C.; Vandezande, W.; Janssen, K. P. F.; Goderis, B.; Debroye, E.; Wang, Y.-K.; Dong, Y.; Ma, D.; Saidaminov, M.; Tan, H.; Lu, Z.; Dyadkin, V.; Chernyshov, D.; Van Speybroeck, V.; Sargent, E. H.; Hofkens, J.; Roeffaers, M. B. J. Thermal Unequilibrium of Strained Black $CsPbI_3$ Thin Films. *Science* **2019**, *365*, 679–684.

(23) Bollyn, M. DMSO Can Be More than a Solvent: Thermal Analysis of Its Chemical Interactions with Certain Chemicals at Different Process Stages. *Org. Process Res. Dev.* **2006**, *10* (6), 1299–1312.

(24) Deguchi, Y.; Kono, M.; Koizumi, Y.; Izato, Y.; Miyake, A. Study on Autocatalytic Decomposition of Dimethyl Sulfoxide (DMSO). *Org. Process Res. Dev.* **2020**, *24* (9), 1614–1620.

(25) Schrode, B.; Pachmajer, S.; Dohr, M.; Rothel, C.; Domke, J.; Fritz, T.; Resel, R.; Werzer, O. GIDVis: A Comprehensive Software Tool for Geometry-Independent Grazing-Incidence X-Ray Diffraction Data Analysis and Pole-Figure Calculations. *J. Appl. Crystallogr.* **2019**, *52* (3), 683–689.

(26) Horcas, I.; Fernández, R.; Gómez-Rodríguez, J. M.; Colchero, J.; Gómez-Herrero, J.; Baro, A. M. WSXM: A Software for Scanning Probe Microscopy and a Tool for Nanotechnology. *Rev. Sci. Instrum.* **2007**, *78* (1), 013705.